DFT insights into the electronic structure, mechanical behaviour, lattice dynamics and defect processes in the first Sc-based MAX phase Sc2SnC

Hadi, M. A., Christopoulos, S., Chroneos, A., Naqib, S. H. & Islam, A. K. M. A

Published PDF deposited in Coventry University's Repository

Original citation:
Hadi, MA, Christopoulos, S, Chroneos, A, Naqib, SH & Islam, AKMA 2022, 'DFT insights into the electronic structure, mechanical behaviour, lattice dynamics and defect processes in the first Sc-based MAX phase Sc2SnC', Scientific Reports, vol. 12, 14037. https://doi.org/10.1038/s41598-022-18336-z

DOI 10.1038/s41598-022-18336-z
ISSN 2045-2322

Publisher: Nature Research

This article is licensed under a Creative Commons Attribution 4.0 International License, which permits use, sharing, adaptation, distribution and reproduction in any medium or format, as long as you give appropriate credit to the original author(s) and the source, provide a link to the Creative Commons licence, and indicate if changes were made. The images or other third party material in this article are included in the article's Creative Commons licence, unless indicated otherwise in a credit line to the material. If material is not included in the article's Creative Commons licence and your intended use is not permitted by statutory regulation or exceeds the permitted use, you will need to obtain permission directly from the copyright holder.

scientific reports

Check for updates

OPEN

DFT insights into the electronic structure, mechanical behaviour, lattice dynamics and defect processes in the first Sc-based MAX phase Sc_2SnC

M. A. Hadi[1]✉, S.-R. G. Christopoulos[2], A. Chroneos[3,4], S. H. Naqib[1] & A. K. M. A. Islam[1,5]

Here we employed the density functional theory calculations to investigate some physical properties of first Sc-based MAX phase Sc_2SnC including defect processes to compare with those of existing M_2SnC phases. The calculated structural properties are in good agreement with the experimental values. The new phase Sc_2SnC is structurally, mechanically and dynamically stable. Sc_2SnC is metallic with a mixture of covalent and ionic character. The covalency of Sc_2SnC including M_2SnC is mostly controlled by the effective valence. Sc_2SnC in M_2SnC family ranks second in the scale of deformability and softness. The elastic anisotropy level in Sc_2SnC is moderate compared to the other M_2SnC phases. The hardness and melting point of Sc_2SnC, including M_2SnC, follows the trend of bulk modulus. Like other members of the M_2SnC family, Sc_2SnC has the potential to be etched into 2D MXenes and has the potential to be a thermal barrier coating material.

Compounds of the ternary laminated family, discovered six decades ago as the H-phases, are now referred to as the MAX phases[1,2]. This family is chemically represented by $M_{n+1}AX_n$, where M is a transition metal, A is an A-group element and X is either carbon or nitrogen or boron[3]. The integer n is called the layer index of the M atom. According to n, the MAX phase family is divided into six sub-families so far, such as 211, 312, 413, 514, 615, and 716 MAX phases[3]. This family has also been described as metallic ceramics because they possess many metallic and ceramic properties[3]. Similar to metals, some MAX phases are electrically and thermally conductive, resistant to thermal shock, damage tolerant, and readily machinable. Again, they resemble ceramics, as some of them are lightweight, wear resistant, elastically rigid, brittle, and resistant to oxidation and corrosion.

The crystal structure of MAX phases consists of nearly close-packed layers of MX_6 octahedra interpolated with square-planar slabs of A-atomic layers. In these the X atoms occupy the octahedral sites between the M-atoms. The A atoms reside in the center of trigonal prisms, which are slightly larger than the octahedral sites and can therefore better accommodate the relatively large A-atoms[4]. The interposing pure A-element planes are mirror planes to the zigzagging $M_{n+1}X_n$-slabs. Alternatively, the structure of the MAX phases consists of highly symmetrical unit cells that are atomically layered along the c-axis. In the unit cell, the $(n+1)$ ceramic MX-layers are stacked along the c-axis between the two metallic A-layers. The thickness of these atomic layers is within the nanometer range and this is the reason MAX phases are sometimes termed as nanolaminates. The periodic arrangement of the metallic and ceramic layers is the reason for the metallic and ceramic properties of the MAX phases. MAX phases have numerous potential applications ranging from aerospace to nuclear reactors[5]. Recently, MAX phases are used to synthesize the two-dimensional MXenes, which are being used as energy storage materials and as electrodes in electrochemical capacitors, micro-supercapacitors, and batteries[6–9].

Interest in the Sn-containing MAX phase is considerable in the community because of the report on attractive electrochemical performance of Nb_2SnC in Li-ion electrolytes[7]. Importantly, two of the three MAX phases discovered after this report are Sn-based MAX Phases. These new members in MAX family are V_2SnC[10], Zr_2SeC[11],

[1]Department of Physics, University of Rajshahi, Rajshahi 6205, Bangladesh. [2]Faculty of Engineering, Environment and Computing, Coventry University, Priory Street, Coventry CV1 5FB, UK. [3]Department of Electrical and Computer Engineering, University of Thessaly, 38221 Volos, Greece. [4]Department of Materials, Imperial College, London SW7 2AZ, UK. [5]International Islamic University Chittagong, Kumira, Chittagong 4318, Bangladesh. ✉email: hadipab@gmail.com

and Sc_2SnC[12]. The last one is the first Sc-based MAX phase reported with full crystallographic information. Previously, Sc_2InC was included into a list for H-phases in a paper[13], however, without any crystallographic data and the source were mentioned as private communication. Up to now there is no experimental evidence for the synthesis and characterization of Sc_2InC. Therefore, it can be inferred that Sc_2SnC is the first Sc-based compound in MAX family. On the other hand, there are six 211 MAX carbides containing Sn as A-site element with different M atoms. These are V_2SnC, Lu_2SnC, Ti_2SnC, Nb_2SnC, Hf_2SnC and Zr_2SnC. These phases are studied extensively and their possible applications are predicted in different studies. Kanoun et al. have studied the mechanical, electronic, chemical bonding and optical properties of Ti_2SnC, Zr_2SnC, Hf_2SnC and Nb_2SnC using DFT[14]. Bouhemadou has conducted a theoretical study of the pressure effect on the structural and elastic properties of M_2SnC (M = Ti, Zr, Nb, Hf) phases[15]. Hadi et al. have investigated the electronic structures, bonding natures and defect processes in the five Sn-based 211 MAX phases[4]. The mechanical behavior, lattice thermal conductivity and vibrational properties of Lu_2SnC MAX phase have also been investigated[16]. The V_2SnC MAX phase is theoretically predicted as a chemically stable, damage and radiation tolerant TBC material[17]. Sc_2SnC is exceptional among the M_2SnC phases as its M-element Sc is a rare-earth element, which, in general, in the MAX compounds is typically a transition metal. Therefore, Sc_2SnC is unique among the M_2SnC MAX phases. This motivated the present DFT investigation which aims to consider all existing Sn-based 211 MAX phase carbides, so as to understand the role of M-elements on the physical properties of a particular A-atom based MAX carbides. Here we systematically calculated the structural, electronic, mechanical, and thermal properties including Vickers hardness and defect processes of Sc_2SnC. The derived properties are compared with those found for previously synthesized M_2SnC MAX phases so as to facilitate comparison and explore the deviation of properties of Sc_2SnC among the existing M_2SnC MAX phases.

Computational methods

The DFT calculations were executed with the CASTEP code[18]. The Perdew-Burke-Ernzerhof (PBE) functional in the frame of generalized gradient approximation (GGA) was employed to estimate the electronic exchange–correlation energy[19]. Ultra-soft pseudo-potential developed by Vanderbilt was used to model the interactions between electrons and ion cores[20]. The Monkhorst–Pack (MP) scheme with a Γ-centered k-point mesh of $15 \times 15 \times 3$ grid is employed to integrate over the first Brillouin zone in the reciprocal space of hexagonal unit cell of Sc_2SnC[21]. A cutoff energy of 700 eV was chosen to expand the eigenfunctions of the valence and nearly valence electrons using a plane-wave basis. During the geometry optimization, both the total energy and internal forces were minimized with the Broyden-Fletcher-Goldfarb-Shanno (BFGS) algorithm[22]. To achieve the self-consistent convergence the difference in the total energy is kept less than 5×10^{-6} eV/atom, the maximum ionic Hellmann–Feynman force less than 0.01 eV/Å, maximum ionic displacement less than 5×10^{-4} Å, and maximum stress less than 0.02 GPa.

The elastic properties are investigated using finite-strain theory as embedded in the CASTEP code[23]. In this method, a predetermined value for strain is used to relax all the free parameters and compute the stress. For elastic calculations, the convergence criteria are set as: the difference in total energy less than 10^{-6} eV/atom, the maximum ionic Hellmann–Feynman force less than 2×10^{-3} eV/Å, and the maximum ionic displacement less than 10^{-4} Å. The finite-strain theory as implemented in CASTEP has been successfully employed to calculate the elastic properties of numerous systems[24–35].

Lattice dynamic properties such as phonon dispersion and phonon density of states are calculated using a $3 \times 3 \times 1$ supercell defined by cutoff radius of 5.0 Å employing the finite displacement supercell method within the code. A $35 \times 35 \times 7$ k-point mesh was used to calculate the electronic charge density distribution and the Fermi surface. Defect calculations were carried out with a $3 \times 3 \times 1$ supercell of 72-atomic site (36 M, 18A, and 18 C) under constant pressure. To determine the potential interstitial sites a thorough computational search was performed examining all potential interstitial sites. The calculations with large supercell require comparatively small cutoff energy and moderate k-point mesh. A cutoff energy of 350 eV and a k-point mesh of $3 \times 3 \times 1$ grid in the MP scheme are used for the supercell defect calculations.

Results and discussions

Structural properties. Commonly with other MAX phases Sc_2SnC crystallizes in the hexagonal space group $P6_3/mmc$ (No. 194)[12]. Each unit cell of Sc_2SnC contains two formula units and eight atoms (refer to Fig. 1a). The Sc atoms occupy the 4f Wyckoff site with the fractional coordinates (1/3, 2/3, z), the Sn resides in the 2*d* atomic site with the fractional coordinates (1/3, 2/3, 3/4) and the C atoms are accommodated at the 2a Wyckoff position with the fractional coordinates (0, 0, 0). The atomic sites of Sc_2SnC with theses fractional coordinates are also valid for all 211 MAX phases. The optimized lattice parameters are listed in Table S1 in the supplementary section along with those of all M_2SnC MAX phases including experimental values[10,12,16,17,36]. The predicted values for Sc_2SnC are very good agreement with the experimental values, supporting the validity of the present investigation. In previous studies[16,17], we observed that the lattice constants of Sn-based 211 MAX phases maintain a good relation with the crystal radius of M-atoms. Both lattice constants *a* and *c* increase almost linearly with the crystal radius of M-atoms. The Sn-based new compound Sc_2SnC also maintains this relationship (see Fig. 1b and c).

Electronic properties. Electronic band structure, electronic density of states (DOS), charge density map, Fermi surface, Mulliken population analysis are investigated to describe the electronic and bonding features of Sc_2SnC, a compound in M_2SnC MAX family.

Band structure and DOS. The electronic band structure of Sc_2SnC was calculated along the high symmetry directions in the first Brillouin zone (refer to Fig. 2a). It reveals the metallic characteristics of Sc_2SnC,

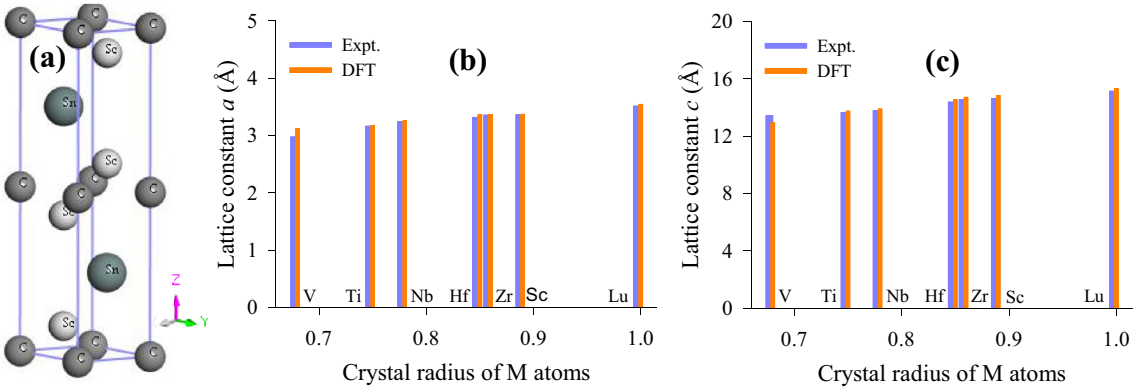

Figure 1. (**a**) Conventional unit cell of Sc_2SnC as a structural model of 211 M_2SnC MAX phases; (**b**) lattice constants *a* and (**c**) lattice constants *c* increase with crystal radius of M atoms.

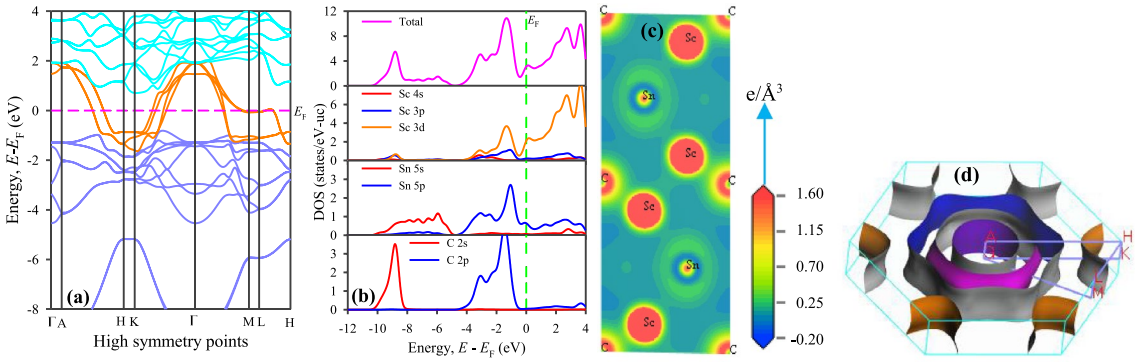

Figure 2. (**a**) Band structure, (**b**) Density of states, (**c**) Charge density map and (**d**) Fermi surface of Sc_2SnC.

which are similar to other MAX phases including M_2SnC as the valence band crosses the Fermi level E_F and overlaps with the conduction band. The Fermi level of Sc_2SnC intersects the crossing bands roughly along the middle and is located at about equal energies from both the pure valence and conduction bands. Conversely, the Fermi level in V_2SnC and Ti_2SnC lies just below the valence band maximum nearby the Γ-point[4,17]. The Γ-point, where most of the valence bands accumulate, shifts upwards for other M_2SnC MAX phases (see Fig. 6 in Ref. 4). The distance of this point from the Fermi level increases following the order: $Ti_2SnC < V_2SnC < Nb_2SnC < Zr_2SnC < Hf_2SnC < Sc_2SnC < Lu_2SnC$. The band features of the Sc_2SnC are very similar to that of the Lu_2SnC compared to other M_2SnC phases[4]. A notable feature in the band structure is the considerable anisotropic nature with low energy dispersion along the c-axis. This is apparent from the reduced dispersion along the short H–K and M–L directions. The anisotropic nature of the band structure near and below the Fermi level indicates that the electrical conductivity is as anisotropic for the Sc_2SnC as for the other M_2SnC MAX phases.

To obtain more information on the chemical bonding in Sc_2SnC, the total and partial densities of states were calculated (refer to Fig. 2b). In this figure, the broken vertical green line refers to the Fermi level E_F, which is located to the left of a pseudogap in the total DOS. It is one of the indications of the structural stability of Sc_2SnC. The proximity of E_F to the pseudogap can lead to more structural stability of the compounds of mixed bonding character[37,38]. Comparing the position of E_F relative to the pseudogap for all existing M_2SnC MAX phases the structural stability should follow the order: $Nb_2SnC > Ti_2SnC > Lu_2SnC > Zr_2SnC > Hf_2SnC > Sc_2SnC > V_2SnC$. The main contribution to the total DOS at E_F comes from the d-orbital of Sc. The d-resonance at the surroundings of E_F and the finite value of the total DOS at E_F indicates the metallic character of Sc_2SnC and this is a common feature of MAX phases. The total DOS of Sc_2SnC at E_F is 3.10 states/eV-uc, which is about half of V_2SnC (6.12 states/eV-uc) and between the range (2.35–3.93 states/eV-uc) of other M_2SnC phases[4,17]. Above the E_F, the antibonding states arise due to d-orbitals of M atom in Sc_2SnC in similar to other M_2SnC MAX phases.

The valence band of Sc_2SnC is divided into two main parts. The lower part is situated between −10.4 eV and −4.9 eV, which contains a distinct peak and a flat region. The peak originates as a result of hybridization between Sc 3d and C 2s orbitals, indicating covalent Sc–C bonding. The flat region arises due to the main contribution of Sn 5s electrons. The upper valence band consists of two distinct peaks. The highest peak close to E_F is also due to the hybridization of Sc 3d electrons with C 2p electrons. Hybridization between Sc 3p and Sn 5p near the E_F also contributes to the highest peak of the total DOS. This hybridization leads to the formation of the Sc-Sn covalent bond between Sc and Sn. This bond is not as strong as Sc-C because the corresponding peak is closer to the Fermi level. The lowest peak centered at −3.3 eV arises due to the interaction between Sc 3d and C 2p states.

The bonding nature of Sc_2SnC is almost same of other M_2SnC MAX phases. Overall, the bonding character in Sc_2SnC is a combination of metallic, covalent, and, owing to the difference in electronegativity between the comprising elements, ionic like other MAX phase compounds.

Charge density. The contour map of the electron charge distribution among the constituent atoms in a compound is a way to understand the nature of atomic bonding in the material. The contour map for Sc_2SnC is given in Fig. 2c. It can be observed that the charge distributions around the atoms have created an almost spherical electron cloud and its intensity determines the amount of charge accumulation. The amount of charge accumulated around the Sc atom is 0.53e, while the amount of charge accumulated around the M atom of other M_2SnC phases is between 0.28 and 0.45e[4,17]. Clearly, the maximum charge accumulates around the Sc atom among all M-atoms in M_2SnC phases. The minimum charge accumulates around Hf[4]. The electron cloud of Sc-charge overlaps with that of C-charge and slightly edges with that of Sn-charge, which indicates the stronger covalent Sc–C and weaker covalent Sc–Sn bonding, respectively. The spherical distribution of charge around the atoms is an indication of some ionic character in chemical bonds in Sc_2SnC. The contour map of electron charge distribution for Sc_2SnC is almost identical to those of other M_2SnC phases.

Fermi surface. The Fermi surface (FS), one of the most innovative ideas developed by solid-state physicists in the last century, isolates occupied electron states from unoccupied ones at zero temperature. The dynamical properties of an electron on the FS commonly depend on where it is found on the FS, and the shape of the FS in regard to the Brillouin zone can assist as a guide to the electrical properties of a metallic system. Currently, the existence of a FS is likely the utmost significant signature of the entity of Fermi liquid quasiparticles in a material. Indeed, the FS is linked to a variety of fascinating physical phenomena. The FS of Sc_2SnC was calculated and is shown in Fig. 2d. The FS consists of four Fermi sheets centered along the Γ–A direction. The three Fermi sheets close to the center of the Brillouin zone have cylindrical or prismatic-like hexagonal cross sections. These are 2D-like electron sheets. The remaining sheet consists of six separate parts parallel to the H–K directions. This sheet is hole-like and situated at the corners of the Brillouin zone around the H–K directions. In comparison to the FSs of M_2SnC family, the FS of Sc_2SnC is very similar to that of Lu_2SnC and simple enough compared to the FSs of other M_2SnC phases[4,17]. The non-spherical shape of the Fermi sheets is an indication of the metallic conductivity of Sc_2SnC[39].

Mulliken population. Population analysis in CASTEP is carried out using a projection of the planewave (PW) states onto a linear combination of atomic orbitals (LCAO) localized basis using a method developed by Sanchez-Portal et al.[40]. Population analysis of the resultant projected states is then accomplished using the Mulliken formalism[41]. This analysis provides the Mulliken charge, bond population and bond length in a bulk material. Mulliken charge associated with a given atom, A, can be determined as:

$$Q(A) = \sum_k \omega_k \sum \sum_{\mu}^{onA} \sum_{\nu} P_{\mu\nu}(k) S_{\mu\nu}(k) \sum \tag{1}$$

where $P_{\mu\nu}(k)$ is the density matrix and $S_{\mu\nu}(k)$ is overlap matrix. The bond population between two atoms A and B can be calculated as:

$$P(AB) = \sum_k \omega_k \sum \sum_{\mu}^{onA} \sum_{\nu}^{onB} 2P_{\mu\nu}(k) S_{\mu\nu}(k) \tag{2}$$

The Mulliken charge measures the effective valence from the absolute difference between the formal ionic charge and the Mulliken charge on the atomic species. Table S2 lists the effective valence, bond population, and bond length between different atoms in Sc_2SnC and existing M_2SnC MAX phases. The pure valence states for transition metals Sc, Ti, V, Zr, Nb, Lu, and Hf in M_2SnC MAX phases are $3d^1$, $3d^2$, $3d^3$, $4d^2$, $4d^4$ $5s^1$, $5d^1$, $5d^2$, respectively. It is observed that the effective valence largely depends on the d-orbital electrons of the transition metals. It increases when the transition metal moves from the left to the right in the periodic table. Its non-zero positive value is an indication of mixed covalent and ionic nature in chemical bonds. Its progression towards zero value indicates an increase in the level of ionicity. Its zero value implies an ideal ionic character in a chemical bond. Its progression from zero with a positive value indicates an increase in covalency level of chemical bonds. Based on the effective valence the covalency of M_2SnC increase when M atoms move from the left to the right in the periodic table.

Bond population is another indication of bond covalency in a crystal as a high value of bond population in essence indicates a high degree of covalency in the chemical bond. The M–C bond in the MAX phases is mainly covalent bond. The bond population of M–C bond in each M_2SnC MAX phases is positive except in Lu_2SnC. The bond population of M–C bond in M_2SnC deceases when the M atom moves from the left to the right in the periodic table, indicating the decrease in covalency. Actually, effective valence and positive bond population collectively control the covalency of crystalline solids. The bulk modulus is mostly controlled by the bond covalency. Between effective valence and positive bond population, which is most influential in bond covalency? This can be verified with the bulk modulus. It is observed from the Fig. 4a in the next section that the bulk modulus changes according to the effective valence. Therefore, it can be concluded that the effective valence mainly controls the covalency level in the studied compounds. The bond length of covalent M–C bond deceases when the M atom moves from the left to the right in the periodic table. It is clear that the shorter the covalent bond length, the

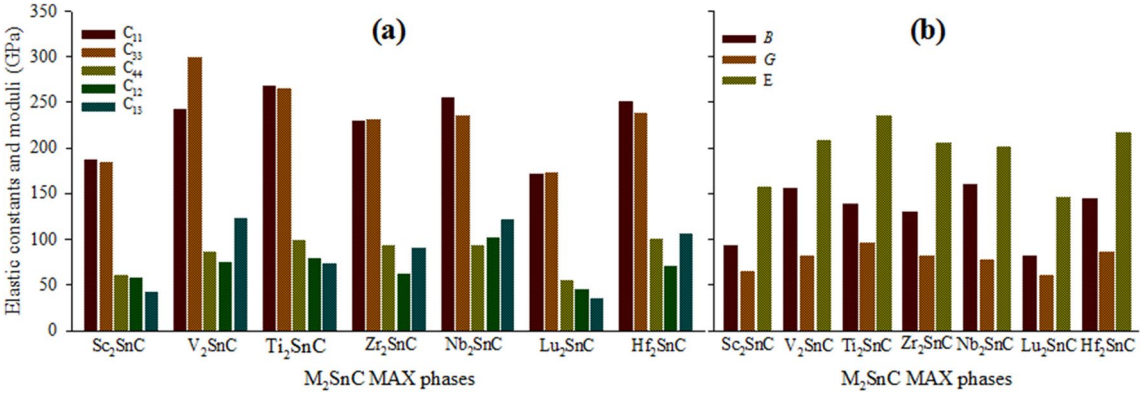

Figure 3. (**a**) Elastic constants C_{ij} and (**b**) elastic moduli B, G, and E of Sc_2SnC and other MAX phases.

higher the bond covalency. A negative bond population indicates the antibonding state between two relevant atoms, which weakens the chemical bonding between them. Other bonds in M_2SnC MAX phases have negative bond population with the exception of the M-Sn bond in Sc_2SnC and the Sn–C bond in Lu_2SnC. Indeed, the Sn–C bond is the only source of the covalency in Lu_2SnC.

Mechanical properties. Single crystal elastic constants, bulk elastic moduli, elastic anisotropy, Vickers hardness are calculated to describe the mechanical behaviors of Sc_2SnC in comparison to existing M_2SnC phases.

Single crystal elastic constants. Elastic constants are the fundamental tools for accessing the mechanical behavior of crystalline solids. MAX phases have five independent elastic constants C_{ij} due to their hexagonal crystal symmetry. These are C_{11}, C_{33}, C_{44}, C_{12} and C_{13}. In addition they have one more dependent elastic constant C_{66}, which depends on C_{11} and C_{12} and $C_{66} = (C_{11}-C_{12})/2$. First of all, the elastic constants justify the mechanical stability of compounds obeying Born criteria. For hexagonal systems these criteria are as follows[42]:

$$C_{11},\ C_{33},\ C_{44} > 0;\ C_{11} > |C_{12}| \text{ and } (C_{11} + C_{12})C_{33} > 2C_{13}C_{13} \quad (3)$$

The calculated elastic constants of Sc_2SnC are listed in Table S3 and shown in Fig. 3a along with CASTEP-derived elastic constants for existing M_2SnC phases for comparison. Sc_2SnC meets the above conditions by its elastic constants like its predecessors M_2SnC and ensures its own mechanical stability like its predecessors.

The elastic constants C_{11} and C_{33} represent the resistance to linear compression, whereas other constants such as C_{12}, C_{13}, and C_{44} represent the resistance to shape change. Indeed, C_{11} and C_{33} represent the stiffness along the crystallographic a- and c-axis, respectively. The stiffness of Sc_2SnC is slightly larger along the a-axis than along the c-axis, which is also observed for Ti_2SnC, Nb_2SnC and Hf_2SnC. For the remaining M_2SnC phases, V_2SnC, Zr_2SnC, and Lu_2SnC, the stiffness along the c-axis is slightly larger than that in the a-axis. The difference between C_{11} and C_{33} quantifies the level of elastic anisotropy in crystals relating to the crystallographic axis. Accordingly, V_2SnC, Nb_2SnC, and Hf_2SnC are elastically more anisotropic than Sc_2SnC, Ti_2SnC, Zr_2SnC, and Lu_2SnC. The new phase Sc_2SnC ranks fourth in the view of both less and high anisotropy in the M_2SnC family of seven members.

Shear elastic constants C_{12} and C_{13} reciprocally lead to a functional stress component along the crystallographic a-axis with a uniaxial strain along the crystallographic b- and c-axis, respectively. This stress component takes the measurements of the shear deformation resistance of a compound along the crystallographic b- and c-axis, when stress is applied along the a-axis. The Nb_2SnC phase is most capable of resisting such deformation, whereas Lu_2SnC will easily deform under an equal stress along the a-axis. The new compound Sc_2SnC will be the second in rank in M_2SnC systems that will be easily deformed if a rank of deformation resistance of M_2SnC system is made: $Nb_2SnC > V_2SnC > Hf_2SnC > Ti_2SnC > Zr_2SnC > Sc_2SnC > Lu_2SnC$.

The elastic constant C_{44} provides an indirect measure of the indentation hardness of a material. A low value of C_{44} indicates higher shearability and low hardness of a compound. High shearability and low hardness are related to better machinability of a compound. Due to low value of C_{44}, Lu_2SnC has highest shearability among the seven M_2SnC MAX phases. The new material Sc_2SnC should be the second in rank in the M_2SnC systems for shearability.

The symmetry condition $C_{66} = (C_{11}-C_{12})/2$ represents an important consequence in hexagonal crystals. C_{66} serves as the shear constant on the (100) plane in a [010] direction, while $(C_{11}-C_{12})/2$ stands for the shear constant on the (110) plane in a [110] direction. Therefore, the elastic shear constant is the same for all planes in the [001] zone, independent on the specific shear plane or shear direction, which is known as the transverse isotropy. This means that the elastic constants are invariant for arbitrary rotation around the z-axis: in the xy plane, the hexagonal crystals are elastically isotropic, which we will observe in a subsequent section.

Bulk elastic moduli. Elastic moduli are the most important elastic parameters that assess the mechanical behavior of crystalline solids. Calculated elastic moduli are listed in Table S3 and shown in Fig. 3b. Bulk modulus B and shear modulus G can be derived from the elastic constants C_{ij} using Voight–Reuss–Hill approximations[43–45]. A detailed discussion of these methods for hexagonal crystals is found in a recent study[46]. The bulk modulus of

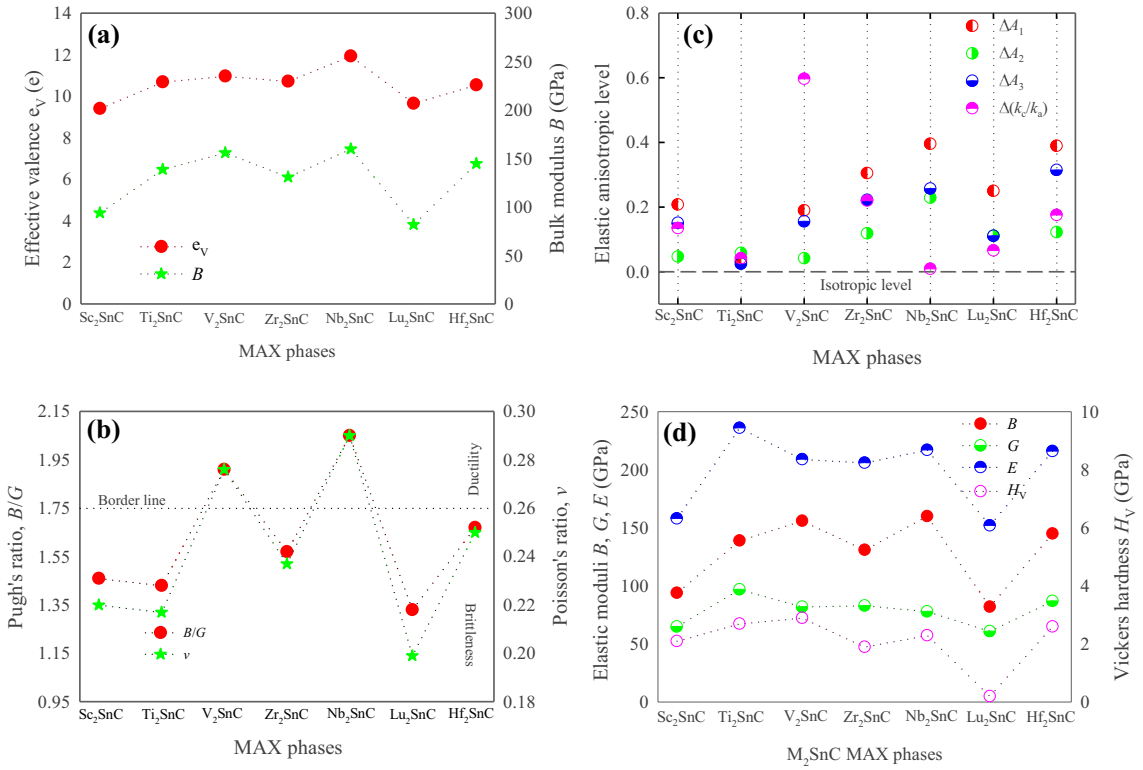

Figure 4. (**a**) Bulk modulus with effective valence; (**b**) Pugh's and Poisson's ratio; (**c**) elastic anisotropy level and (**d**) Vickers hardness with elastic moduli of M_2SnC.

a crystal depends microscopically on the nature of its bond such as length and type. In the case of the studied compound it is observed that it is also controlled by the total effective valence of the crystal (see Fig. 4a). Bulk modulus is a measure of the resistance to uniform compression of a material and it is linked to chemical composition and crystal structure. Among M_2SnC phases, the new phase Sc_2SnC possesses the second lowest value for B. The highest value is assigned to Nb_2SnC and the lowest value is associated with Lu_2SnC. Therefore, Sc_2SnC will be compressed more easily as compared to existing M_2SnC phases except Lu_2SnC. The shear modulus G is concerned with the deformation of a solid material when it experiences a force parallel to one of its surfaces while its opposite face experiences an opposing force such as friction. G maintains a good relationship with C_{44}. Here, it is reflected and Sc_2SnC secure the second rank in the scale of lowest value of G similar to C_{44}.

B and G collectively prescribe an important parameter known as Pugh's ratio (defined as B/G) that evaluates a necessary mechanical behavior of crystalline solids[47]. Generally, a material is either considered brittle or ductile. The brittle materials have a value less than 1.75 and ductile materials possess a value greater than 1.75. Materials with a B/G value above or below this borderline value behave in a less ductile or brittle manner. Accordingly, Sc_2SnC is a brittle material similar to Ti_2SnC, Zr_2SnC, Lu_2SnC and Hf_2SnC while V_2SnC and Nb_2SnC exhibit ductility (refer to Fig. 4b).

Poisson's ratio ν is another important parameter and can be derived from B and G: $\nu = (3B-2G)/(6B+2G)$. Similar to Pugh's ratio, Poisson's ratio can serve as a predictor for distinguishing brittle from ductile materials. Poisson's ratio ν with a value less than 0.26 identifies the materials as brittle ones and with a higher value the ductile ones[48]. The Poisson's ratio has classified the M_2SnC MAX phases into brittle and ductile groups, consistently with Pugh's ratio above. That is, the Sc_2SnC can be considered brittle. The Poisson's ratio can also identify the interatomic forces between atoms in a solid[49]. When the Poisson's ratio of a solid is between 0.25 and 0.50, the interatomic forces between the atoms of that solid will be the central forces and if the Poisson's ratio is outside of this range the interatomic forces will be the non-central forces[50]. A central force is a force (possibly negative) that points directly from a particle to a certain point in space, the center and whose magnitude depend only on the distance of the particle from the center while a non-centrifugal force is a force between two particles that is not directed along their connecting line. The Poisson's ratio of V_2SnC, Hf_2SnC and Nb_2SnC lies in this range and accordingly their interatomic forces are central forces i.e., these compounds are stabilized with the central forces and they are called central-force solids. For central force solids the Cauchy relations are generally established. The interatomic forces in the new phase Sc_2SnC including remaining M_2SnC phases are non-central forces as their Poisson's ratios are outside this range. Consequently, Sc_2SnC, Zr_2SnC, Ti_2SnC and Lu_2SnC are stabilized with the non-central forces and they are called non-central-force solids. For non-central-force solids the Cauchy relations are generally not established. Moreover, the Poisson's ratio can predict the bonding nature in solids[51]. A completely covalent crystal is characterized with a Poisson's ratio equal or less than 0.1. A perfectly metallic compound possesses a Poisson's ratio equal or greater than 0.33. The Poisson's ratio of Sc_2SnC including

existing M_2SnC lies between 0.1 and 0.33, indicating that their chemical bonding is a combination of metallic and covalent natures.

Elastic moduli B and G also provide another essential property, the Young's modulus E via the relation, $E = 9BG/(3B + G)$. The Young's modulus of a material is a useful property for predicting the behaviour of the material when subjected to a tensile force. Stiffness of a material mostly depends on its Young's modulus. Higher Young's modulus is an indication of higher stiffness. In the family of M_2SnC MAX phases, Ti_2SnC is the stiffest material and Lu_2SnC is the softest one. The newly synthesized Sc_2SnC ranks second on the scale of softness: $Lu_2SnC > Sc_2SnC > Nb_2SnC > Zr_2SnC > V_2SnC > Hf_2SnC > Ti_2SnC$. The Young's modulus of MAX phases can be related to the exfoliation energy. The smaller the Young's modulus, the softer the system and hence the lower the exfoliation energy and the higher the possibility of etching into 2D MXenes[52]. The four MAX phases Ti_2AlC, Ti_2AlN, V_2AlC, and Nb_2AlC in the 211 family are exfoliated experimentally into MXenes[53]. Their theoretical Young's moduli[54] range from 262 to 312 GPa and exfoliation energies[53] range from 0.164 to 0.205 eV/Å^2. V_2AlC has the highest Young's modulus (~ 312 GPa) and consequently has the highest exfoliation energy (0.205 eV/Å^2). As the Young's moduli of the Sn-based 211 MAX phases under study range from 152 to 219 GPa, their exfoliation energies can be expected to be lower than 0.205 eV/Å^2. Very recently, the exfoliation energies of Sc_2SnC, Ti_2SnC, V_2SnC, Zr_2SnC, Nb_2SnC, and Hf_2SnC are calculated to be 0.131, 0.164, 0.137, 0.157, 0.150, and 0.158 eV/Å^2, respectively[55]. These values lie within the range between 0.131 and 0.164 eV/Å^2, which are lower than the range of 0.164 and 0.205 eV/Å^2. As the Young's modulus of Lu_2SnC is lowest in the M_2SnC phases considered here, its exfoliation energy can be expected to lie within this range. The lower the exfoliation energy, the higher the possibility to be etched experimentally into 2D MXenes. Therefore, Lu_2SnC and other M_2SnC phases considered here are more likely to be etched into 2D MXenes than V_2AlC. Further, the Young's modulus E has a good relation to the thermal shock resistance R: $R \propto 1/E$[56]. The lower the Young's modulus, the better the thermal shock resistance. A material of higher thermal shock resistance (i.e., lower Young's modulus) has the potential to be used as a TBC material. The Young's modulus of Sc_2SnC and other M_2SnC MAX phases are lower than that of a potential TBC material TiO_2 whose Young modulus is 283 GPa[57]. Therefore, Sc_2SnC and other existing M_2SnC phases have possibility to be TBC materials if they also have high thermal expansion coefficient and melting point, low thermal conductivity, and good oxidation resistance.

Elastic anisotropy. The study of elastic anisotropy is important as it influences a variety of physical processes including the development of plastic deformation in crystals, microscale cracking in ceramics, and plastic relaxation in thin-film metallics[58]. For hexagonal crystals like MAX phases the shear anisotropy factors A_i (i = 1, 2, 3) are studied extensively[16,27,28,31,59]. The equation that determines the shear anisotropy factor A_1, for the {100} shear planes between the < 011 > and < 010 > directions, is $A_1 = (C_{11} + C_{12} + 2C_{33}4C_{12})/6C_{44}$; the equation of A_2, for the {010} shear planes between < 101 > and < 001 > directions, is $A_2 = 2C_{44}/(C_{11}C_{12})$; and the equation of A_3, for the {001} shear planes between < 110 > and < 010 > directions, is $A_3 = (C_{11} + C_{12} + 2C_{33}4C_{13})/3(C_{11}C_{12})$. Deviation of A_i from unity ΔA_i ($= A_i \sim 1$) quantifies the degree of shear anisotropy of crystals. The calculated A_i is listed in Table S4 and the anisotropy level ΔA_i is shown in Fig. 4c. Considering the average on all the planes, Ti_2SnC is elastically less anisotropic and Nb_2SnC is elastically highly anisotropic. Sc_2SnC ranks third in view of less anisotropy in the M_2SnC family: $Nb_2SnC > Hf_2SnC > Zr_2SnC > Lu_2SnC > Sc_2SnC > V_2SnC > Ti_2SnC$. Individually, in the {100} shear planes Nb_2SnC is highly anisotropic; in the {010} shear planes Nb_2SnC is again highly anisotropic and in the {001} shear planes Hf_2SnC is highly anisotropic.

The anisotropy level in the hexagonal crystals like MAX phases can also be quantified by another anisotropy factor named compressibility anisotropy factor and it is defined as $k_c/k_a = (C_{11} + C_{12}2C_{13})/(C_{33}C_{13})$[48]. Here, k_a and k_c are the linear compressibility coefficients along the a- and c-axis, respectively. Deviation of k_c/k_a from the unity $\Delta(k_c/k_a)$ ($= k_c/k_a \sim 1$) quantifies the degree of the compressibility anisotropy of crystals. The calculated k_c/k_a is listed in Table S4 and $\Delta(k_c/k_a)$ is shown in Fig. 4c. The compressibility anisotropy level is highest in V_2SnC and lowest in Nb_2SnC. Sc_2SnC ranks in the middle in the M_2SnC family of seven members. If $k_c/k_a > 1$, the material is more compressible along the c-axis than along the a-axis. Therefore, Sc_2SnC, Ti_2SnC and Lu_2SnC are slightly more compressible along the c-axis than along the a-axis while V_2SnC, Zr_2SnC, Nb_2SnC and Hf_2SnC are compressed more easily along the a-axis than along the c-axis.

There are some anisotropy factors such as percentage anisotropy factors $A_{B\%}$ and $A_{G\%}$ based on the bulk and shear moduli within the Voigt and Reuss limits, which are applicable for all types of crystals. $A_{B\%}$ measures anisotropy in compression while $A_{G\%}$ measures anisotropy in shear. These two factors are defined as $A_{B\%} = [(B_V B_R)/(B_V + B_R)] \times 100\%$ and $A_{G\%} = [(G_V G_R)/(G_V + G_R)] \times 100\%$[51]. The calculated values are listed in Table S4. Both these factors assign zero value for isotropic crystals and their positive values indicate the anisotropy level in crystals. $A_{B\%}$ is highest for V_2SnC and lowest for Ti_2SnC while $A_{G\%}$ is highest for Hf_2SnC and lowest for Ti_2SnC. Sc_2SnC ranks fourth on the $A_{B\%}$ scale and second on the $A_{G\%}$ scale in terms of minimum anisotropy. Universal anisotropy factor A^U is also applicable for all types of crystals. It is defined as $A^U = 5(G_V/G_R) + (B_V/B_R)6 \geq 0$[17]. Its zero value corresponds to isotropic crystals and a positive value implies the anisotropy level in crystals. The calculated values are listed in Table S4. Hf_2SnC has the highest value of A^U and Ti_2SnC possesses the lowest value. Sc_2SnC has the second lowest value of A^U.

The 2D and 3D graphical representations of the directional elastic properties of materials are visualization of elastic anisotropy in crystals. ELATE is an open-source software[60], which allows the direct visualization of anisotropy level in Young's modulus (E), linear compressibility (β), shear modulus (G) and Poisson's ratio (ν) on the 3D spherical plot, as well as 2D projections on the (xy), (xz) and (yz) planes. Uniform circular 2D and spherical 3D graphical representations are the indications of isotropic nature of crystals. As the MAX phases are hexagonal crystals, they are elastically isotropic in the xy plane. It is evident that the 2D presentation of E, β, G and ν of Sc_2SnC in the xy plane in Fig. 5 are uniformly circular, indicating the isotropic nature of elastic

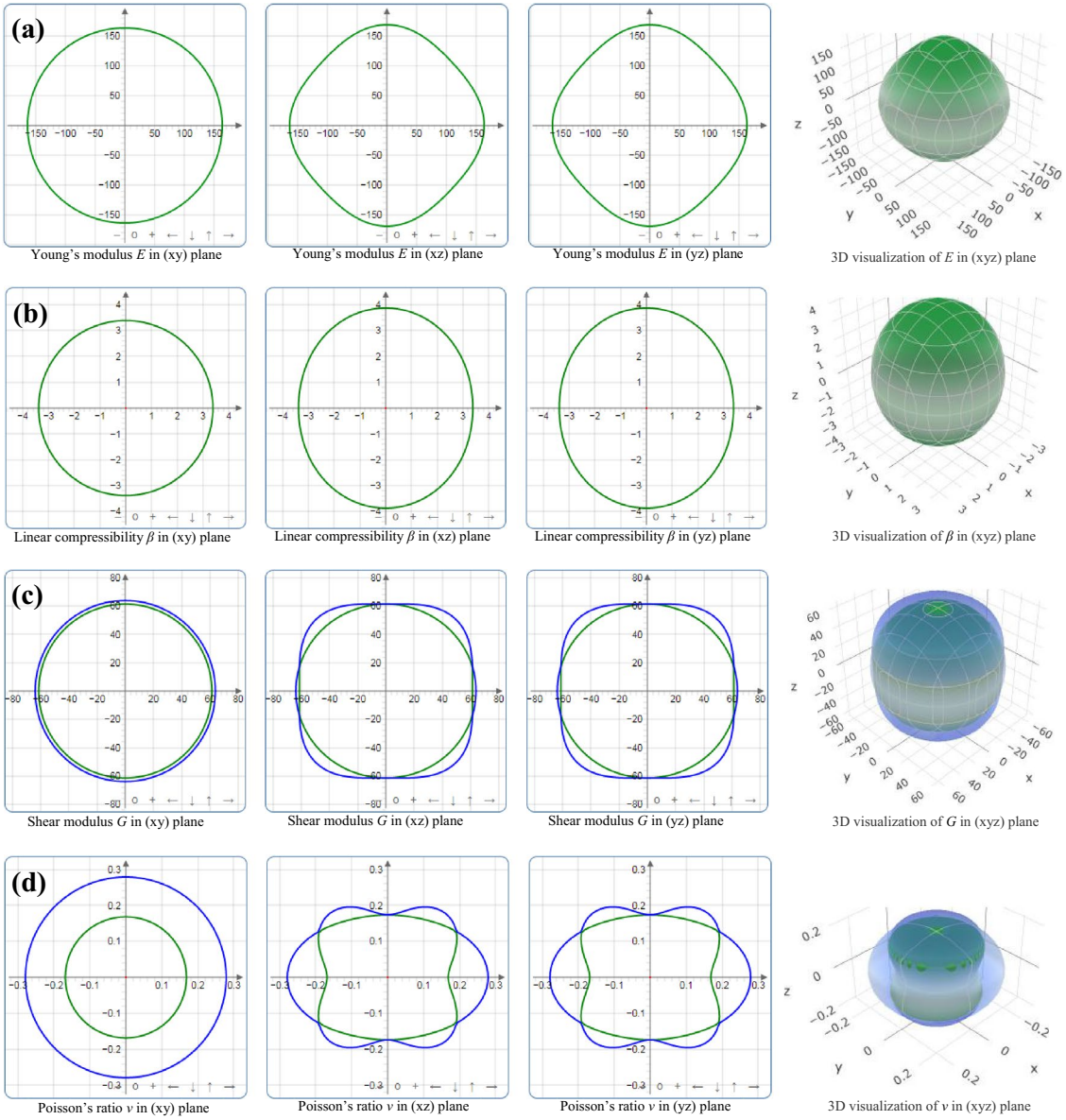

Figure 5. Directional dependence of (**a**) Young's modulus *E*, (**b**) linear compressibility β, (**c**) shear modulus *G* and (**d**) Poisson's ratio *ν* of Sc_2SnC.

properties of Sc_2SnC in xy plane. The 2D presentation of *E*, *β*, *G* and *ν* of Sc_2SnC in the xz and yz planes in Fig. 5 is indicating the elastic anisotropy of Sc_2SnC in those planes. The greater the deviation from the round shape, the higher the anisotropy level in the crystals in that plane.

In 2D and 3D presentations, ELATE uses maximum two colors for *E* and β and maximum three colors for *G* and *ν*. The *E* and β are functions of a single unit vector $\mathbf{a}(\theta, \phi)$ while *G* and *ν* depend on two orthogonal unit vectors $\mathbf{a}(\theta, \phi)$ and $\mathbf{b}(\theta, \phi, \chi)$ (**a** in the direction of the stress applied while **b** in the direction of measurement). The spherical coordinates θ, ϕ, and χ can be defined as $0 \leqslant \theta \leqslant \pi$, $0 \leqslant \phi \leqslant 2\pi$, and $0 \leqslant \chi \leqslant 2\pi$. Therefore, *E*, β, *G* and *ν* can be expressed as $E(\theta, \phi)$, $\beta(\theta, \phi)$, $G(\theta, \phi, \chi)$ and $\nu(\theta, \phi, \chi)$. $G(\theta, \phi, \chi)$ and $\nu(\theta, \phi, \chi)$ are represented in 3D space via plotting two surfaces *f* and *g* each with the spherical (θ, ϕ) coordinates. The surfaces *f* and *g* represent the minimal and maximal values over all possible values of χ: $f(\theta, \phi) = \min_{\chi} X(\theta, \phi, \chi)$ and $g(\theta, \phi) = \max_{\chi} X(\theta, \phi, \chi)$, respectively. The surface *g* encloses the surface *f*. For this reason, *g* is plotted in translucent blue color in Fig. 5. The surface *f* is represented with solid green color for positive values and translucent red color for negative values. The absence of red color implies that there are no negative values for *E*, β, *G* and *ν* of Sc_2SnC in any direction. The directional dependencies of *E*, β, *G* and *ν* on the xz and yz planes are almost identical for Sc_2SnC, similar to Nb_2SnC, Hf_2SnC and Zr_2SnC MAX phases[17]. Ti_2SnC displays almost isotropic nature of *E*, β, *G* and *ν* in the xz and yz planes. The directional dependence of *E*, β, *G*, and *ν* in the Lu_2SnC differs from that of other M_2SnC phases. For Sc_2SnC, Ti_2SnC and Lu_2SnC, β has almost no directional dependence.

ELATE imparts a quantitative analysis reporting the minimum and maximum values of each modulus along with the directions along which these extrema occur. It also allows determining the directions of special interest

Phases	Young's modulus (GPa)		Linear compressibility (TPa^{-1})		Shear modulus (GPa)		Poisson's ratio	
	E_{min}	E_{max}	β_{min}	β_{max}	G_{min}	G_{max}	ν_{min}	ν_{max}
Sc_2SnC	152.13	168.70	3.383	3.868	61.39	70.89	0.174	0.279
V_2SnC	188.79	223.85	1.096	2.711	71.36	86.67	0.129	0.388
Hf_2SnC	168.97	236.44	1.958	2.481	66.85	99.80	0.122	0.390
Lu_2SnC	143.59	167.39	3.831	3.959	56.84	70.09	0.166	0.264
Nb_2SnC	168.47	237.13	1.778	2.149	66.30	97.20	0.153	0.417
Ti_2SnC	233.72	239.43	2.415	2.451	95.41	100.21	0.194	0.225
Zr_2SnC	174.63	222.77	2.140	2.789	68.42	94.74	0.136	0.338
Elastic anisotropy A_X								
	A_E		A_β		A_G		A_ν	
Sc_2SnC	1.109		1.143		1.155		1.605	
V_2SnC	1.186		2.473		1.215		3.022	
Hf_2SnC	1.399		1.267		1.493		3.195	
Lu_2SnC	1.166		1.033		1.233		1.589	
Nb_2SnC	1.408		1.208		1.466		2.730	
Ti_2SnC	1.024		1.015		1.050		1.159	
Zr_2SnC	1.276		1.303		1.385		2.483	

Table 1. Minimal and maximal values of each modulus and elastic anisotropy of Sc_2SnC and existing M_2SnC[16,17].

for elastic properties, which are not required to be along the crystallographic axes of the material. Additionally, it reports a measurement of the anisotropy A_X of each elastic modulus X, which is defined below:

$$A_X = \begin{cases} X_{\max}/X_{\min} & \text{if } \operatorname{sign}(X_{\max}) = \operatorname{sign}(X_{\min}) \\ \infty & \text{otherwise} \end{cases} \tag{4}$$

The results are listed in Table 1. It is evident that Young's modulus exhibits maximum anisotropy for Nb_2SnC and minimum for Ti_2SnC and Sc_2SnC ranks second in view of minimum anisotropy. Anisotropy in linear compressibility is maximum for V_2SnC and minimum for Ti_2SnC; Sc_2SnC ranks third in scale of minimum anisotropy. Anisotropy in shear modulus is highest for Hf_2SnC and lowest for Ti_2SnC; Sc_2SnC ranks second in view of minimum anisotropy. Maximum anisotropy of Poisson's ratio is observed in Hf_2SnC and minimum in Ti_2SnC, whereas Sc_2SnC ranks third in view of minimum anisotropy. The lowest anisotropy is observed for Ti_2SnC in the M_2SnC family considering all indicators.

Theoretical hardness. Hardness is the property of a material that facilitates it to resist plastic deformation, penetration, indentation and scratching. Therefore, hardness is important from an engineering point of view because the resistance to wear by either abrasion or corrosion by steam, oil and water usually increases with hardness. Theoretical modeling for hardness calculation of partially metallic compounds like ternary MAX phases is difficult. Gou et al. developed a model[61] based on Mulliken bond population[41] that is able to calculate the theoretical Vickers hardness of MAX phases. According to this model the bond hardness can be calculated as:

$$H_v^\mu = 740\left(P^\mu - P^{\mu'}\right)\left(v_b^\mu\right)^{-5/3} \tag{5}$$

where P^μ denotes to the positive Mulliken bond overlap population of the μ-type bond, $P^{\mu'}$ represents the metallic population that is derived from the unit cell volume V and the number of free electrons in the cell, n_{free} with the formula, $P^{\mu'} = \frac{n_{free}}{V}$, here $n_{free} = \int_{E_P}^{E_F} N(E)dE$ and E_P and E_F define the energies at the pseudogap and at the Fermi level, respectively, and v_b^μ is the bond volume of a μ-type bond calculated using the equation $v_b^\mu = (d^\mu)^3 / \sum_\mu \left[(d^\mu)^3 N_b^\mu\right]$, here d^μ and N_b^μ are respectively the bond length and bond number of μ type bonds per unit volume.

When a compound has a positive bond population for multiple bonds, the following equation is used to calculate its Vickers hardness:

$$H_V = [\prod_{\mu}^{\mu}(H_v^\mu)^{n^\mu}]^{1/\sum n^\mu} \tag{6}$$

where n^μ represents the number of μ-type bonds. Table S5 lists the Vickers hardness of Sc_2SnC and other M_2SnC MAX phases. Sc_2SnC is harder than Lu_2SnC and Zr_2SnC and softer than Ti_2SnC, V_2SnC, Nb_2SnC and Hf_2SnC. We have found two sets of experimental Vickers hardness for Ti_2SnC, Zr_2SnC, Hf_2SnC, and Nb_2SnC[36,62]. Experimental values show deviations from one set to another except for Ti_2SnC. This can be due to sample purity and errors induced by the instruments. Furthermore, the experiment is performed with a sample that contains

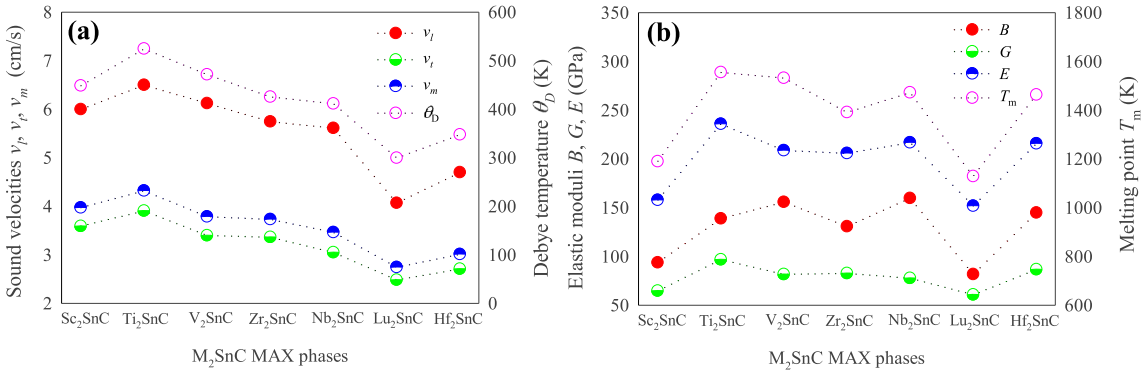

Figure 6. (**a**) Debye temperature with sound velocities; (**b**) melting temperature with elastic moduli.

grains. The grain size largely controls the plasticity as well as the hardness of the compounds. The experimental temperature may be another reason. Although the theoretical values deviate from the experimental values they remain within the typical values (2–8 GPa) for MAX phases. Lu_2SnC has a low value for H_v, which is very small compared to the lower limit (2 GPa) for the MAX phases. The reason may be the absence of covalent M–C bonds in Lu_2SnC. Indeed, all M_2SnC phases have low hardness compared to most of the MAX phases. Consequently, M_2SnC phases are soft compared to other MAX phases.

In general, the hardness of a compound has a better relationship with its shear and Young's modulus than bulk modulus[3]. We have plotted the Vickers hardness of M_2SnC MAX phases in Fig. 4d along with their elastic moduli. For the M_2SnC MAX phases, it is observed that the hardness follows the trend of bulk modulus instead of shear and Young's modulus. Further verification is needed to determine whether this trend continues for the carbide MAX phase with a specific A-group element.

Lattice dynamics. The subject of lattice dynamics is the study of the vibrations of the atoms in a crystal. The vibrations of the atoms are related to many important physical properties such as lattice thermal conductivity, minimum thermal conductivity, Debye temperature, melting point, phonon dispersion, phonon DOS etc. These properties are investigated for newly synthesized Sc_2SnC to compare with existing M_2SnC phases.

Debye temperature. Debye temperature is a characteristic temperature at which the highest-frequency mode (and hence every possible mode) is excited. It is related to many physical properties such as thermal expansion, thermal conductivity, specific heat and lattice enthalpy. The Anderson method is simple and rigorous way to calculate the Debye temperature of crystalline materials using the equation[63]:

$$\theta_D = \frac{h}{k_B}\left[\left(\frac{3n}{4\pi}\right)\frac{N_A\rho}{M}\right]^{1/3} v_m \tag{7}$$

All symbols bear the conventional meanings and v_m refers to the average sound velocity, which can be determined using the following equation:

$$v_m = \left[\frac{1}{3}\left(\frac{1}{v_l^3} + \frac{2}{v_t^3}\right)\right]^{-1/3} \tag{8}$$

Here, v_l and v_t are the longitudinal and transverse sound velocities, respectively. They can be calculated from the bulk and shear moduli B and G using the equations:

$$v_l = \left(\frac{3B + 4G}{3\rho}\right)^{1/2} \text{ and } v_t = \left(\frac{G}{\rho}\right)^{1/2} \tag{9}$$

The calculated values of θ_D for M_2SnC MAX phases are listed in Table S6 along with the relevant quantities. The Debye temperature of Sc_2SnC is the third highest in the M_2SnC family. In this family, Ti_2SnC possesses the highest Debye temperature and Lu_2SnC has the lowest Debye temperature. The Debye temperature of M_2SnC phases largely depends on the sound velocities and follows the trend of change of sound velocities with the transition metal M (refer to Fig. 6a).

Melting point. Melting point of hexagonal crystals like MAX phases can be calculated from elastic constants using: $T_m = 354 + 1.5(2C_{11} + C_{33})$[64]. The calculated values are listed in Table S6. The new phase Sc_2SnC possesses the second lowest melting point. The highest melting point is obtained for Ti_2SnC and the lowest melting point is observed for Lu_2SnC. A higher melting point indicates greater interatomic forces in crystals. Interatomic forces mainly control the bulk elastic properties of crystalline solids. Thus, a relationship can exist between the elastic modulus and the melting temperature of the crystals. Considering this we plotted the elastic moduli and the

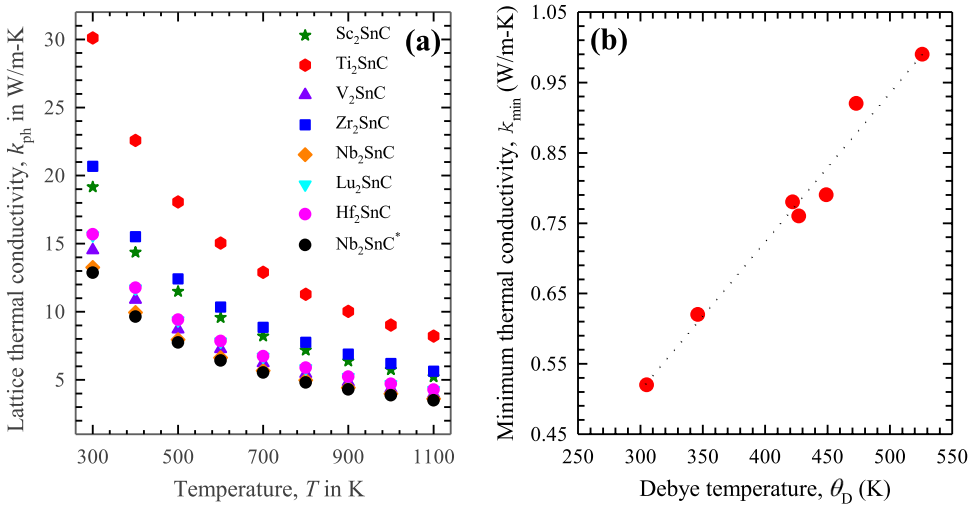

Figure 7. (**a**) Lattice thermal conductivity as a function of temperature. Theoretical data for Nb_2SnC are taken from Ref. 59*; (**b**) minimum thermal conductivity as a function of Debye temperature.

melting point of M_2SnC MAX phases in Fig. 6b. It is observed that the melting point has better correlation with bulk modulus B and Young's modulus E than shear modulus G.

Lattice thermal conductivity. The lattice thermal conductivity arises from contributions of phonons of all frequencies. The knowledge of lattice thermal conductivity is important to determine the applicability of a material for use in high temperature environments. Recently, room temperature lattice thermal conductivity of two MAX phases Zr_2SeC and Zr_2SC are reported, which are 75 and 80.7% of the total thermal conductivity of the compounds, respectively[11]. So, the lattice thermal conductivity of metallic compounds like MAX phases provides the concept of total thermal conductivity in a computationally tractable way. For this reason, many authors have reported lattice thermal conductivity of many compounds including MAX phases[11,65–68] Encouraged by these reports we have calculated the lattice thermal conductivity of the newly synthesized Sc_2SnC MAX phase. Here, the Slack model is used to calculate the lattice thermal conductivity of Sc_2SnC as MAX phases have dual characteristics of metals and ceramics[69]. The following equation is used in this model:

$$k_{\mathrm{ph}} = A\frac{M_{\mathrm{av}}\theta_D^3\delta}{\gamma^2 n^{2/3} T} \tag{10}$$

The details of this model are given in a recent study[70]. The room temperature lattice thermal conductivity of Sc_2SnC and other M_2SnC phases are listed in Table S6 and their temperature dependency is shown in Fig. 7a. The Debye temperature of the M_2SnC phases is calculated to range from 300 to 525 K. This implies that all vibrational modes will be active above these temperatures for the M_2SnC MAX phases. Consequently, from these temperatures and above the phonon contribution becomes dominant in the total thermal conductivity. Here, we report the lattice thermal conductivity of M_2SnC MAX phases in the temperature range of 300 to 1100 K. In this temperature range, the electronic contribution to the total thermal conductivity should be insignificant. The room temperature (300 K) thermal conductivity of 60 W K^{-1} m^{-1}, measured in Ti_2SC is the highest to date, despite the fact that its electrical conductivity (1.926×10^6 Ω^{-1} m^{-1}) is relatively poor. This is due to the large contribution from phonons[71]. For the temperatures at and above 300 K, the lattice contribution should dominate the total thermal conductivity of MAX phases. For comparison, we have the literature values for lattice thermal conductivity of Nb_2SnC[65], which are also plotted in Fig. 7. The present values show good agreement with the literature values. It is observed that Sc_2SnC has the third highest lattice thermal conductivity in the entire temperature range and Ti_2SnC and Nb_2SnC possess the highest and lowest values, respectively. The lattice thermal conductivity of M_2SnC MAX phases decrease gradually with the increase of temperature. The rate of decrease is almost similar for all M_2SnC phase. Sc_2SnC should be suitable candidate as a TBC material as other M_2SnC phases are[17].

Minimum thermal conductivity. Thermal conductivity decreases with increasing temperature. Thus, the minimum value of thermal conductivity is significant for the application of materials at high temperature conditions, for instance, materials selection and design for thermoelectric, thermal barrier coating and other thermal management applications. The concept of a minimum thermal conductivity, κ_{min}, carried by the atomic vibrations of any solid material led to the development of different models. The Clarke model has become popular for determining the minimum thermal conductivity of solids via the Eq.[72]:

$$\kappa_{\mathrm{min}} = k_{\mathrm{B}}\nu_{\mathrm{m}}\left(\frac{nN_{\mathrm{A}}\rho}{M}\right)^{2/3} \tag{12}$$

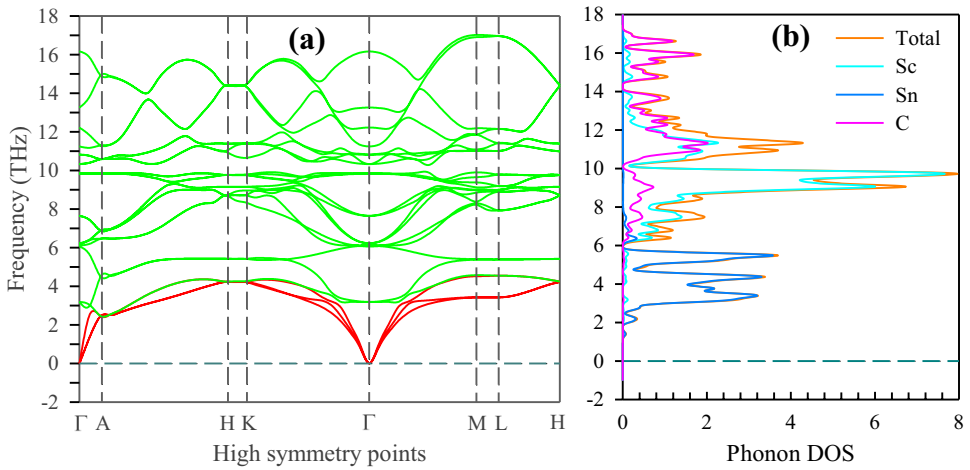

Figure 8. (**a**) Phonon dispersion and (**b**) Phonon DOS.

All symbols in Eq. (12) are consistent to the symbols used in Eq. (7). The calculated value of κ_{min} is listed in Table S6. The phase Sc_2SnC has the third highest value for κ_{min}. The highest value is found for V_2SnC and the lowest value is observed for Lu_2SnC. The ultralow minimum thermal conductivity of 1.25 W/m–K is used for screening the appropriate materials for TBC application[73]. The values of κ_{min} for M_2SnC MAX phases are lower than this optimum value. Therefore, all M_2SnC phases should be promising TBC materials with greater possibility for Lu_2SnC. The minimum thermal conductivity has a linear correlation with the Debye temperature for M_2SnC phases (Fig. 7b).

Phonon dispersion and phonon DOS. It is important to study the phonon dispersion and phonon density of states (DOS) to verify the dynamical stability of the crystalline solids. The calculated phonon dispersion is shown in Fig. 8a. For a dynamically stable crystal, there are always three phonons with zero frequency at Γ-point, which corresponds to $k=0$ in reciprocal space. The phonon branches starting at $\omega(k)=0$ are called acoustic phonon dispersion curves[74]. In the case of Sc_2SnC (refer to Fig. 8a) the acoustic branches start at $\omega(k)=0$ and consequently indicate the dynamical stability of Sc_2SnC. The phonons, whose frequencies are non-zero at the Γ point, are called optical phonons. In a number of high-symmetry crystals, and along the high-symmetry directions, the atomic vibrations are either polarized along the propagation wave vector k, or perpendicular to k. Acoustic modes have one longitudinal acoustic (LA) mode, and two transverse acoustic (TA) modes. A crystal consisting of a unit cell of N-atoms has $3N$–3 optical modes. Accordingly, 211 MAX phases have 21 optical modes. In the Fig. 8a, the acoustic branches are shown with red and optical branches are identified with green.

The calculated phonon DOS of Sc_2SnC is shown in Fig. 8b, revealing that the acoustic and the lower optical modes arise due to the vibration of heavier Sn-atoms. The middle optical branches arise due to the vibration of Sc-atoms. The higher optical branches mostly originate from the vibration of lighter C-atoms. Acoustic phonon is caused by the coherent vibrations of atoms in a lattice outside their equilibrium position. Conversely, the optical phonon originates due to the out-of-phase oscillation of the atom in the lattice when an atom moves to the left and its neighbor to the right. Most of the optical properties of the crystals are controlled by the optical phonons.

Zone-center phonon modes are of particular interest in the lattice dynamics of crystal solids. Since the Sn-based 211 MAX phases consist of 8 atoms, they have 24 phonon branches or vibration modes. Three of these are acoustic modes with zero frequency at Γ-point and the remaining 21 are optical modes. Of these 21 optical modes, six are IR active, seven are Raman active and the remaining eight are silent modes. Consistent with the factor group theory, the irreducible representations of the Brillouin zone-center optical phonon modes can be classified as:

$$\Gamma_{opt.} = 2A_{2u} + 4E_{1u} + 2E_{1g} + 4E_{2g} + A_{1g} + 2B_{1u} + 2B_{2g} + 4E_{2u}$$

where A_{2u} and E_{1u} are IR active and A_{1g}, E_{1g} and E_{2g} are Raman active and B_{1u}, B_{2g} and E_{2u} are silent modes. The total modes obtained for the M_2SnC phases in this study are consistent with previous theoretical studies of the lattice dynamics of the various 211 MAX phases[75–77]. Each mode has a specific frequency of vibration. Sometimes two or more modes have the same frequency but it cannot be claimed that they are distinct modes; these modes are called degenerate. For this reason, Table 2 contains six IR active modes and seven Raman active modes. The highest frequencies of the IR active modes are observed at 442.5, 546.3, 621.9, 503.5, 576.0, 459.8 and 600.2 cm^{-1} for Sc_2SnC, Ti_2SnC, V_2SnC, Zr_2SnC, Nb_2SnC, Lu_2SnC and Hf_2SnC, respectively, while the highest Raman active modes for these compounds are observed at 407.7, 372.1, 274.7, 224.3, 275.0, 171.8 and 179.5 cm^{-1}, respectively.

Defect processes. The motivation to examine the point defect processes of materials stems from the fact that they can impact the macroscopic materials properties (i.e. radiation tolerance)[78–80]. In that respect the investiga-

Mode		Irr. Rep	Wavenumbers ω (cm^1)						
			Sc_2SnC	Ti_2SnC	V_2SnC	Zr_2SnC	Nb_2SnC	Lu_2SnC	Hf_2SnC
IR	ω_1	A_{2u}	201.9	263.0	110.0	197.2	198.4	145.2	186.0
	ω_2	E_{1u}	207.5	223.6	105.1	119.0	127.8	75.7	87.7
	ω_3	E_{1u}	344.8	535.7	621.9	495.3	576.0	339.9	600.2
	ω_4	A_{2u}	442.5	546.3	560.1	503.5	537.6	459.8	558.0
Raman	ω_1	E_{2g}	106.1	65.4	96.2	67.4	65.8	68.7	73.8
	ω_2	E_{2g}	328.0	365.8	257.6	192.7	211.6	110.2	133.8
	ω_3	E_{1g}	328.6	372.1	260.8	202.2	220.9	109.7	138.5
	ω_4	A_{1g}	407.7	347.7	274.7	224.3	275.0	171.8	179.5

Table 2. Theoretical wavenumbers ω and symmetry assignment of the IR-active and Raman-active modes of the Sn-based M_2SnC MAX phases.

	Reaction (V denotes vacancy)	Defect energy (eV)						
		Sc_2SnC	V_2SnC	Lu_2SnC	Ti_2SnC	Zr_2SnC	Hf_2SnC	Nb_2SnC
1	$M_M \rightarrow V_M + M_i$	7.35	6.40	6.61	8.75	8.66	9.34	8.70
2	$Sn_{Sn} \rightarrow V_{Sn} + Sn_i$	4.21	7.95	3.57	8.97	6.63	7.51	7.56
3	$C_C \rightarrow V_C + C_i$	3.33	5.12	2.23	6.10	5.34	4.68	5.18
4	$M_M + Sn_{Sn} \rightarrow M_{Sn} + Sn_M$	3.98	4.67	3.67	4.92	4.83	4.72	5.12
5	$M_M + C_C \rightarrow M_C + C_M$	11.31	9.37	11.79	12.81	15.40	16.37	12.64
6	$Sn_{Sn} + C_C \rightarrow Sn_C + C_{Sn}$	8.52	8.64	7.75	9.98	9.64	10.07	10.05
7	$Sn_i + V_M \rightarrow Sn_M$	− 4.57	− 5.17	− 3.61	− 6.86	− 4.71	− 5.17	− 4.34
8	$C_i + V_M \rightarrow C_M$	− 1.65	− 0.80	− 0.13	− 1.07	0.12	1.47	− 0.48
9	$M_i + V_{Sn} \rightarrow M_{Sn}$	− 3.01	− 4.51	− 2.90	− 5.94	− 5.75	− 6.96	− 6.79
10	$C_i + V_{Sn} \rightarrow C_{Sn}$	1.26	0.03	1.56	− 0.19	0.22	0.89	− 0.10
11	$M_i + V_C \rightarrow M_C$	2.27	− 1.35	3.08	− 0.97	1.28	0.88	− 0.76
12	$Sn_i + V_C \rightarrow Sn_C$	− 0.29	− 4.46	0.39	− 4.91	− 2.55	− 3.01	− 2.58
13	$M_i + Sn_{Sn} \rightarrow M_{Sn} + Sn_i$	1.20	3.44	0.67	3.03	0.88	0.55	0.76
14	$M_i + C_C \rightarrow M_C + C_i$	5.61	3.77	5.31	5.13	6.62	5.56	4.42
15	$Sn_i + M_M \rightarrow Sn_M + M_i$	2.78	1.24	3.01	1.89	3.95	4.17	4.36
16	$Sn_i + C_C \rightarrow Sn_C + C_i$	3.04	0.66	2.62	1.19	2.79	1.67	2.60
17	$C_i + M_M \rightarrow C_M + M_i$	5.70	5.60	6.49	7.69	8.78	10.81	8.22
18	$C_i + Sn_{Sn} \rightarrow C_{Sn} + Sn_i$	5.47	7.98	5.13	8.79	6.85	8.40	7.46
	Schottky reaction	9.78	5.83	9.99	7.97	9.69	8.57	6.70

Table 3. The defect reaction energies as calculated for Sc_2SnC and existing M_2SnC[4,17]MAX phases.

tion of point defects in MAX phases is very important as they can be in radiation environments given that they are considered for nuclear applications[81–83].

Table 3 lists the defect reactions and the corresponding defect energies for Sc_2SnC and the existing M_2SnC MAX phases. In these calculations we have considered all the possible point defects including all the interstitial sites existing in the 211 M_2SnC MAX phases. The preferable sites are shown in Fig. S1. For the defect reactions we employed the Kröger-Vink notation[84]. In this notation M_i stands for an M interstitial defect, V_{Sn} for a Sn vacant site and M_{Sn} an M atom residing in a Sn site (known as antisite defect). Typically, the energies of the Schottky reaction in this system are high (Table 3) and therefore the Frenkel reactions (Table 3, relations 1–3) or the antisite reactions (Table 3, relations 4–6) are more relevant when considering the radiation tolerance of the material. For Sc_2SnC the C-Frenkel energy is only 3.33 eV inferring that this is not a particularly radiation tolerant MAX phase as compared to most of the other MAX phases considered here (Table 3). Commonly, with the other MAX phases in Table 3 there is the possibility to form antisite vacancies via the recombination of self-interstitials and vacancies. For Sc_2SnC this is inferred by the negative energies in reactions 7–9 and 12.

Conclusions

In summary, we have employed DFT calculations to investigate the structural, electronic, mechanical and lattice dynamical properties of Sc_2SnC including defect processes to compare with those of existing M_2SnC MAX phases. The calculated structural properties show fair agreement with the available experimental values. The structural, mechanical and dynamical stability of Sc_2SnC is verified. The chemical bonding of Sc_2SnC is a combination of metallic, covalent and ionic. The softness, elastic anisotropy level and deformability of Sc_2SnC are moderate compared to the other M_2SnC phases. Sc_2SnC has the potential to be etched into 2D MXenes and be a promising

TBC material, similar to the other M_2SnC phases. The hardness of M_2SnC, including Sc_2SnC, follows the trend of bulk modulus rather than shear and Young's modulus while the melting point has a better relationship with the bulk and Young's modulus than with the shear modulus. The rate of declination of lattice thermal conductivity with temperature is almost similar for all M_2SnC phases. The minimum thermal conductivity shows a linear relationship with the Debye temperature. The highest frequency of the IR active modes for Sc_2SnC is lowest in the M_2SnC family while the highest frequency of the Raman active mode is largest for Sc_2SnC. Examining the defect processes of the existing M_2SnC phases it is revealed that Sc_2SnC is less radiation tolerant than numerous 211 MAX phases.

Data availability

All data generated or analysed during this study are included in this published article and its supplementary information files.

Received: 5 January 2022; Accepted: 9 August 2022
Published online: 18 August 2022

References

1. Nowotny, V. H. Strukturchemie einiger Verbindungen der Übergangsmetalle mit den elementen C, Si, Ge, Sn. *Progress Solid State Chem.* **5**, 27–70 (1971).
2. Barsoum, M. W. *MAX Phases: Properties of Machinable Ternary Carbides and Nitrides* (Wiley VCH, 2013).
3. Hadi, M. A. Superconducting phases in a remarkable class of metallic ceramics. *J. Phys. Chem. Solids* **138**, 109275 (2020).
4. Hadi, M. A., Kelaidis, N., Naqib, S. H., Chroneos, A. & Islam, A. K. M. A. Electronic structures, bonding natures and defect processes in Sn-based 211 MAX phases. *Comput. Mater. Sci.* **168**, 203–212 (2019).
5. Zapata-Solvas, E. *et al.* Synthesis and physical properties of $(Zr_{1-x}, T_iX_i)3Al_C2$ MAX phases. *J. Am. Ceram. Soc.* **100**, 3393–3401 (2017).
6. Shuck, C. E. & Gogotsi, Y. MXenes: A tunable family of 2D Carbides and nitrides with diverse applications. *Mater. Matters* **15**, 3–10 (2020).
7. Zhao, S. *et al.* Electrochemical interaction of Sn-containing MAX Phase (Nb_2SnC) with Li-Ions. *ACS Energy Lett.* **4**, 2452–2457 (2019).
8. Ng, V. M. H. *et al.* Recent progress in layered transition metal carbides and/or Nitrides (MXenes) and their composites: Synthesis and applications. *J. Mater. Chem. A* **5**, 3039–3068 (2017).
9. Bai, Y. *et al.* Dependence of elastic and optical properties on surface terminated groups in two-dimensional MXene monolayers: A first-principles study. *RSC Adv.* **6**, 35731–35739 (2016).
10. Xu, Q. *et al.* Theoretical prediction, synthesis, and crystal structure determination of new MAX phase compound V_2SnC. *J. Adv. Ceramics* **9**, 481–492 (2020).
11. Chen, K. *et al.* MAX phase Zr_2SeC and its thermal conduction behavior. *J. Eur. Ceram. Soc.* **41**, 4447–4451 (2021).
12. Li, Y. *et al.* Molten salt synthesis of nanolaminated Sc_2SnC MAX phase. *J. Inorganic Mater.* **36**, 773–778 (2021).
13. Toth, L. E., Jeitschko, W. & Yen, C. M. The superconducting behavior of several complex carbides and nitrides. *J. Less Common Metals* **10**, 29–32 (1966).
14. Kanoun, M. B., Goumri-Said, S. & Reshak, A. H. Theoretical study of mechanical, electronic, chemical bonding and optical properties of Ti_2SnC, Zr_2SnC, Hf_2SnC and Nb_2SnC. *Comp. Mater. Sci.* **47**, 491–500 (2009).
15. Bouhemadou, A. Prediction study of structural and elastic properties under pressure effect of M_2SnC (M = Ti, Zr, Nb, Hf). *Physica B* **403**, 2707–2713 (2008).
16. Hadi, M. A., Kelaidis, N., Naqib, S. H., Chroneos, A. & Islam, A. K. M. A. Mechanical behaviors, lattice thermal conductivity and vibrational properties of a new MAX phase Lu_2SnC. *J. Phys. Chem. Solids* **129**, 162–171 (2019).
17. Hadi, M. A. *et al.* Chemically stable new MAX phase V_2SnC: a damage and radiation tolerant TBC material. *RSC Adv.* **10**, 43783–43798 (2020).
18. Clark, S. J. *et al.* First principles methods using CASTEP. *Zeitschrift für Kristallographie—Crystalline Mater.* **220**, 567–570 (2005).
19. Perdew, J. P., Burke, K. & Ernzerhof, M. Generalized gradient approximation made simple. *Phys. Rev. Lett.* **77**, 3865–3868 (1996).
20. Vanderbilt, D. Soft self-consistent pseudopotentials in a generalized eigenvalue formalism. *Phys. Rev. B* **41**, 7892–7895 (1990).
21. Monkhorst, H. J. & Pack, J. D. Special points for Brillouin-zone integrations. *Phys. Rev. B* **13**, 5188–5192 (1976).
22. Fischer, T. H. & Almlof, J. General methods for geometry and wave function optimization. *J. Phys. Chem.* **96**, 9768–9774 (1992).
23. Murnaghan, F. D. *Finite deformation of an elastic solid* (Wiley, 1951).
24. Hadi, M. A. *et al.* First-principles prediction of mechanical and bonding characteristics of new T2 superconductor Ta_5GeB_2. *Physica Status Solidi(b)* **253**, 2020–2026 (2016).
25. Hadi, M. A. *et al.* Elastic and thermodynamic properties of new $(Zr_{3-x}Ti_x)AlC_2$ MAX-phase solid solutions. *Comput. Mater. Sci.* **137**, 318–326 (2017).
26. Rubel, M. H. K. *et al.* Density functional theory study of a new Bi-based $(K_{1.00})(Ba_{1.00})_3(Bi_{0.89}Na_{0.11})_4O_{12}$ double perovskite superconductor. *Computational Materials Science* **138**, 160–165 (2017).
27. Roknuzzaman, M. *et al.* First hafnium-based MAX phase in the 312 family, Hf_3AlC_2: A first-principles study. *J. Alloy. Compd.* **727**, 616–626 (2017).
28. Nasir, M. T. *et al.* First-principles study of superconducting ScRhP and ScIrP pnictides. *Physica status solidi (b)* **254**, 1700336 (2017).
29. Christopoulos, S.-R.G. *et al.* Intrinsic defect processes and elastic properties of Ti_3AC_2 (A = Al, Si, Ga, Ge, In, Sn) MAX phases. *J. Appl. Phys.* **123**, 025103 (2018).
30. Tanveer Karim, A. M. M. *et al.* Newly synthesized $MgAl_2Ge_2$: A first-principles comparison with its silicide and carbide counterparts. *J. Phys. Chem. Solids* **117**, 139–147 (2018).
31. Hadi, M. A. *et al.* Physical properties and defect processes of M_3SnC_2 (M = Ti, Zr, Hf) MAX phases: Effect of M-elements. *J. Alloy. Compd.* **748**, 804–813 (2018).
32. Hadi, M. A., Islam, M. N. & Babu, M. H. Cubic Perovskite $Pb(Mg_{1/3}Nb_{2/3})O_3$: A damage tolerant machinable, and thermal barrier coating material. *Zeitschrift für Naturforschung A* **74**, 71–81 (2019).
33. Filippatos, P. P. *et al.* 312 MAX Phases: Elastic Properties and Lithiation. *Materials* **12**, (2019).
34. Islam, M. N., Hadi, M. A. & Podder, J. Influence of Ni doping in a lead-halide and a lead-free halide perovskites for optoelectronic applications. *AIP Adv.* **9**, 125321 (2019).
35. Ali, M. M. *et al.* DFT investigations into the physical properties of a MAB phase Cr4AlB4. *J. Alloy. Compd.* **821**, 153547 (2020).
36. Barsoum, M. W., Yaroschuk, G. & Tyagi, S. Fabrication and characterization of M_2SnC (M = Ti, Zr, Hf and Nb). *Scripta Mater.* **37**, 1583–1591 (1997).

37. Ravindran, P. & Asokamani, R. Correlation between electronic structure, mechanical properties and phase stability in intermetallic compounds. *Bull. Mater. Sci.* **20**, 613–622 (1997).
38. Xu, J.-H. & Freeman, A. J. Band filling and structural stability of cubic trialuminides: YAl_3, $ZrAl_3$, and $NbAl_3$. *Phys. Rev. B* **40**, 11927 (1989).
39. Dugdale, S. B. Life on the edge: A beginner's guide to the Fermi surface. *Phys. Scr.* **91**, 053009 (2016).
40. Sanchez-Portal, D., Artacho, E. & Soler, J. M. Projection of plane-wave calculations into atomic orbitals. *Solid State Commun.* **95**, 685–690 (1995).
41. Mulliken, R. S. Electronic population analysis on LCAO–MO molecular wave functions I. *J. Chem. Phys.* **23**, 1833–1840 (1955).
42. Born, M. On the stability of crystal lattices. I. *Math. Proc. Cambridge Philosophical Soc.* **36**, 160–172 (1940).
43. Voigt, W. *Lehrbuch der Kristallphysik* (Taubner, 1928).
44. Reuss, A. Berechnung der Fließgrenze von Mischkristallen auf Grund der Plastizitätsbedingung für Einkristalle. *ZAMM J. Appl. Math. Mech./Zeitschrift für Angewandte Mathematik und Mechanik* **9**, 49–58 (1929).
45. Hill, R. The elastic behaviour of a crystalline aggregate. *Proc. Phys. Soc. Sect. A* **65**, 349–354 (1952).
46. Azzouz-Rached, A. *et al.* Pressure effects on the structural, elastic, magnetic and thermodynamic properties of Mn_2AlC and Mn_2SiC MAX phases. *J. Alloy. Compd.* **885**, 160998 (2021).
47. Pugh, S. F. XCII. Relations between the elastic moduli and the plastic properties of polycrystalline pure metals. *Null* **45**, 823–843 (1954).
48. Hadi, M. A. New ternary nanolaminated carbide Mo_2Ga_2C: A first-principles comparison with the MAX phase counterpart Mo_2GaC. *Comput. Mater. Sci.* **117**, 422–427 (2016).
49. Hadi, M. A. *et al.* Effects of Al substitution by Si in Ti_3AlC_2 nanolaminate. *Sci. Rep.* **11**, 3410 (2021).
50. Fu, H., Li, D., Peng, F., Gao, T. & Cheng, X. Ab initio calculations of elastic constants and thermodynamic properties of NiAl under high pressures. *Comp. Mater. Sci.* **44**, 774–778 (2008).
51. Ali, M. A., Hadi, M. A., Hossain, M. M., Naqib, S. H. & Islam, A. K. M. A. Theoretical investigation of structural, elastic, and electronic properties of ternary boride MoAlB. *Phys. Status Solidi* **254**, 1700010 (2017).
52. Champagne, A. *et al.* Insights into the elastic properties of RE-i-MAX phases and their potential exfoliation into two-dimensional RE-i-MXenes. *Phys. Rev. Mater.* **4**, 013604 (2020).
53. Khazaei, M. *et al.* Insights into exfoliation possibility of MAX phases to MXenes. *Phys. Chem. Chem. Phys.* **20**, 8579–8592 (2018).
54. Aryal, S., Sakidja, R., Barsoum, M. W. & Ching, W.-Y. A genomic approach to the stability, elastic, and electronic properties of the MAX phases. *Physica Status Solidi (b)* **251**, 1480–1497 (2014).
55. Khaledialidusti, R., Khazaei, M., Khazaei, S. & Ohno, K. High-throughput computational discovery of ternary-layered MAX phases and prediction of their exfoliation for formation of 2D MXenes. *Nanoscale* **13**, 7294 (2021).
56. Wang, X. *et al.* Mechanical properties and damage tolerance of bulk $Yb_3Al_5O_{12}$ ceramic. *J. Mater. Sci. Technol.* **31**, 369–374 (2015).
57. Cao, X. Q., Vassen, R. & Stoever, D. Ceramic materials for thermal barrier coatings. *J. Eur. Ceram. Soc.* **24**, 1–10 (2004).
58. Kube, C. M. Elastic anisotropy of crystals. *AIP Adv.* **6**, 095209 (2016).
59. Hadi, M. A., Rayhan, M. A., Naqib, S. H., Chroneos, A. & Islam, A. K. M. A. Structural, elastic, thermal and lattice dynamic properties of new 321 MAX phases. *Comput. Mater. Sci.* **170**, 109144 (2019).
60. Gaillac, R., Pullumbi, P. & Coudert, F.-X. ELATE: An open-source online application for analysis and visualization of elastic tensors. *J. Phys.: Condens. Matter* **28**, 275201 (2016).
61. Gou, H., Hou, L., Zhang, J. & Gao, F. Pressure-induced incompressibility of ReC and effect of metallic bonding on its hardness. *Appl. Phys. Lett.* **92**, 241901 (2008).
62. El-Raghy, T., Chakraborty, S. & Barsoum, M. W. Synthesis and characterization of Hf_2PbC, Zr2PbC and M_2SnC (M=Ti, Hf, Nb or Zr). *J. Eur. Ceram. Soc.* **20**, 2619–2625 (2000).
63. Anderson, O. L. A simplified method for calculating the debye temperature from elastic constants. *J. Phys. Chem. Solids* **24**, 909–917 (1963).
64. Fine, M. E., Brown, L. D. & Marcus, H. L. Elastic constants versus melting temperature in metals. *Scr. Metall.* **18**, 951–956 (1984).
65. Dhakal, C., Aryal, S., Sakidja, R. & Ching, W.-Y. Approximate lattice thermal conductivity of MAX phases at high temperature. *J. Eur. Ceram. Soc.* **35**, 3203–3212 (2015).
66. Ali, M. A. *et al.* Physical properties of new MAX phase borides M_2SB (M = Zr, Hf and Nb) in comparison with conventional MAX phase carbides M_2SC (M = Zr, Hf and Nb): Comprehensive insights. *J. Mater. Res. Tech.* **11**, 1000–1018 (2021).
67. Li, S. *et al.* Pushing the limit of thermal conductivity of MAX borides and MABs. *J. Mater. Sci. Tech.* **97**, 79–88 (2022).
68. Wang, X.-F., Ma, J.-J. & Jiao, Z.-Y. Phase stability, mechanical properties and lattice thermal conductivity of $Ti_2(Al_xSn_{1-x})C$ solid solutions: A DFT study. *Mod. Phys. Let. B.* **30**, 1650413 (2016).
69. Morelli, D. T. & Slack, G. A. High Lattice Thermal Conductivity Solids. in *High Thermal Conductivity Materials* (eds. Shindé, S. L. & Goela, J. S.) 37–68 (Springer New York, 2006). https://doi.org/10.1007/0-387-25100-6_2.
70. Ali, M. M., Hadi, M. A., Ahmed, I., Haider, A. F. M. Y. & Islam, A. K. M. A. Physical properties of a novel boron-based ternary compound Ti_2InB_2. *Mater. Today Commun.* **25**, 101600 (2020).
71. Sun, Z. M. Progress in research and development on MAX phases: a family of layered ternary compounds. *Int. Mater. Rev.* **56**, 143–166 (2011).
72. Clarke, D. R. Materials selection guidelines for low thermal conductivity thermal barrier coatings. *Surf. Coat. Technol.* **163–164**, 67–74 (2003).
73. Liu, Y. *et al.* Discovery of ABO_3 perovskites as thermal barrier coatings through high-throughput first principles calculations. *Null* **7**, 145–151 (2019).
74. Parlinski, K., Lattice Dynamics: Vibrational Modes. *Encyclopedia Condensed Matter Phys.*, 98–102 (2005).
75. Hadi, M. A. *et al.* Insights into the physical properties of a new 211 MAX phase Nb2CuC. *J. Phys. Chem. Solids* **149**, 109759 (2021).
76. Champagne, A. *et al.* Phonon dispersion curves in Cr2AlC single-crystals. *Mater. Res. Lett.* **6**, 378–383 (2018).
77. Akter, K., Parvin, F., Hadi, M. A. & Islam, A. K. M. A. Insights into the predicted Hf_2SN in comparison with the synthesized MAX phase Hf_2SC: A comprehensive study. *Comput. Condensed Matter* **24**, e00485 (2020).
78. Grimes, R. W. *et al.* The effect of ion size on solution mechanism and defect cluster geometry. *Ber. Bunsenges. Phys. Chem.* **101**, 1204–1210 (1997).
79. Sickafus, K. E. *et al.* Radiation tolerance of complex oxides. *Science* **289**, 748 (2000).
80. Chroneos, A., Rushton, M. J. D., Jiang, C. & Tsoukalas, L. H. Nuclear wasteform materials: Atomistic simulation case studies. *J. Nucl. Mater.* **441**, 29–39 (2013).
81. Horlait, D., Grasso, S., Chroneos, A. & Lee, W. E. Attempts to synthesise quaternary MAX phases (Zr, M)2AlC and Zr2(Al, A)C as a way to approach Zr2AlC. *Null* **4**, 137–144 (2016).
82. Zapata-Solvas, E. *et al.* Experimental synthesis and density functional theory investigation of radiation tolerance of $Zr_3(Al_{1-x}Si_x)C_2$MAX phases. *J. Am. Ceram. Soc.* **100**, 1377–1387 (2017).
83. Hanson, W. A., Patel, M. K., Crespillo, M. L., Zhang, Y. & Weber, W. J. Influence of electronic vs nuclear energy loss in radiation damage of Ti_3SiC_2. *Acta Mater.* **161**, 302–310 (2018).
84. Kröger, F. A. & Vink, H. J. Relations between the Concentrations of Imperfections in Crystalline Solids. in *Solid State Physics* (eds. Seitz, F. & Turnbull, D.) **3**, 307–435 (Academic Press, 1956).

Acknowledgements
The authors wish to acknowledge the High-Performance Computing (HPC) facility at Coventry University, Priory Street, Coventry CV1 5FB, UK for providing the computational facility to calculate the defect processes in newly synthesized Sc_2SnC MAX phase.

Author contributions
M.A.H. conceived the study and wrote the main manuscript text. M.A.H. and S.-R.G.C. carried out the calculations and prepared all figures. All authors reviewed the manuscript.

Competing interests
The authors declare no competing interests.

Additional information
Supplementary Information The online version contains supplementary material available at https://doi.org/10.1038/s41598-022-18336-z.

Correspondence and requests for materials should be addressed to M.A.H.

Reprints and permissions information is available at www.nature.com/reprints.

Publisher's note Springer Nature remains neutral with regard to jurisdictional claims in published maps and institutional affiliations.

Open Access This article is licensed under a Creative Commons Attribution 4.0 International License, which permits use, sharing, adaptation, distribution and reproduction in any medium or format, as long as you give appropriate credit to the original author(s) and the source, provide a link to the Creative Commons licence, and indicate if changes were made. The images or other third party material in this article are included in the article's Creative Commons licence, unless indicated otherwise in a credit line to the material. If material is not included in the article's Creative Commons licence and your intended use is not permitted by statutory regulation or exceeds the permitted use, you will need to obtain permission directly from the copyright holder. To view a copy of this licence, visit http://creativecommons.org/licenses/by/4.0/.

© The Author(s) 2022